

***In Situ* Visualization by X-Ray Computed Tomography on Sulfur Stabilization and Lithium Polysulfides Immobilization in S@HCS/MnO<sub>x</sub> Cathode**

Ruoyu Xu <sup>a,+</sup>, Jingwei Xiang <sup>b,+</sup>, Junrun Feng <sup>a</sup>, Xuekun Lu <sup>a</sup>, Zhangxiang Hao <sup>a</sup>, Liqun Kang <sup>a</sup>, Ming Li <sup>b</sup>, Yunsong Wu <sup>a</sup>, Chun Tan <sup>a</sup>, Yiyun Liu <sup>a</sup>, Guanjie He <sup>a</sup>, Dan J.L. Brett <sup>a</sup>, Paul R. Shearing <sup>a,\*</sup>, Lixia Yuan <sup>b,\*</sup>, Yunhui Huang <sup>b,\*</sup>, Feng Ryan Wang <sup>a,\*</sup>

<sup>a</sup> Department of Chemical Engineering, University College London, Torrington Place, WC1E 7JE, London, United Kingdom

<sup>b</sup> State Key Laboratory of Material Processing and Die & Mold Technology, School of Materials Science and Engineering, Huazhong University of Science and Technology, Wuhan 430074, China

\*Corresponding authors' E-mail addresses: p.shearing@ucl.ac.uk (P.R. Shearing); ryan.wang@ucl.ac.uk (F. Wang); yuanlixia@hust.edu.cn (L. Yuan); huangyh@hust.edu.cn (Y. Huang).

<sup>+</sup>These authors contributed equally to this work.

**Abstract:**

The lithium-sulfur (Li-S) batteries have high theoretical energy density, exceeding that of the lithium-ion batteries. However, their practical applications are hindered by the capacity decay due to lithium polysulfide shuttle effect and sulfur volume expansion. Here, we design a S@hollow carbon with porous shell/MnO<sub>x</sub> (S@HCS/MnO<sub>x</sub>) cathode to accommodate and immobilize sulfur and polysulfides, and develop a non-destructive technique X-ray computed tomography (X-ray CT) to *in situ* visualize the volume expansion of Li-S cathode. The designed cathode achieves a specific capacity of ~1100 mAh g<sup>-1</sup> at 0.2 C with a fade rate of 0.18% per cycle over 300 cycles. The X-ray CT shows that only 16% volume expansion and 70% volume fraction of solid sulfur remaining in the S@HCS/MnO<sub>x</sub> cathode, superior to the commercial cathode with 40% volume expansion and 5% volume remaining of solid sulfur particles. This is the first reported visualization evidence for the effectiveness of hollow carbon structure in accommodating cathode volume expansion and immobilizing sulfur shuttling. X-ray CT can serve as a powerful *in situ* tool to trace the active materials and then feedback to the structure design, which helps develop efficient and reliable energy storage systems.

**Keywords:** lithium-sulfur battery; X-ray computed tomography; *in situ* visualization; designed sulfur cathode; electrochemical performance.

## 1. Introduction

The lithium sulfur (Li-S) batteries are considered as the next-generation energy storage systems with key advantages of cost-effectiveness, high theoretical energy density (2500 Wh kg<sup>-1</sup>) and environmental sustainability.[1-8] The practical application of Li-S batteries is hindered by two obstacles: i) 80% volume expansion from sulfur (S<sub>8</sub>) to lithium sulfide (Li<sub>2</sub>S) during cycling, leading to the structure damage of the cathode and the rapid capacity decay;[9, 10] ii) the dissolution of lithium polysulfides (LiPSs) intermediates into electrolyte, causing severe shuttle effect, decreasing the active sulfur and blocking the lithium anode.[10-18] It is therefore important to understand the structural evolution of the cathode and its degradation mechanism. Porous carbon materials with hollow structure have been widely used in cathode to immobilize the active sulfur. The efficiency of such cathode designs is usually proved by post-cycling analysis and the direct visual evidence is yet to be reported.[19, 20] The understanding is a challenge for any post-cycling analysis due to i) the irreversible damage of cathode materials during cell disassembly; ii) sensitive nature of the organic electrolyte and LiPSs.[21-25] Therefore, developing *in situ* analysis and imaging techniques will be crucial to the future of Li-S battery. The lab-used X-ray computed tomography (X-ray CT), as a non-destructive technique, could provide achievable resolution range from 16 nm to tens of microns, corresponding to a recommended sample size from 16 μm to centimetres. Due to this high resolution and wide range of sample size, X-ray CT that has been used in electrode investigation for solid oxide fuel cell,[26, 27] proton exchange membrane fuel cell[28] and Li-ion batteries,[29, 30] providing direct visualization and statistical analysis of electrode microstructure. It visualizes the contrast difference upon X-ray transmission, which is very sensitive to the sulfur element due to its large atomic numbers comparing to lithium and carbon. Here we use X-ray CT to prove the efficiency of as-designed S@hollow carbon

sphere (HCS)/MnO<sub>x</sub> cathode for the accommodation and immobilization of active sulfur under *in situ* operation conditions (**Fig. 1**).

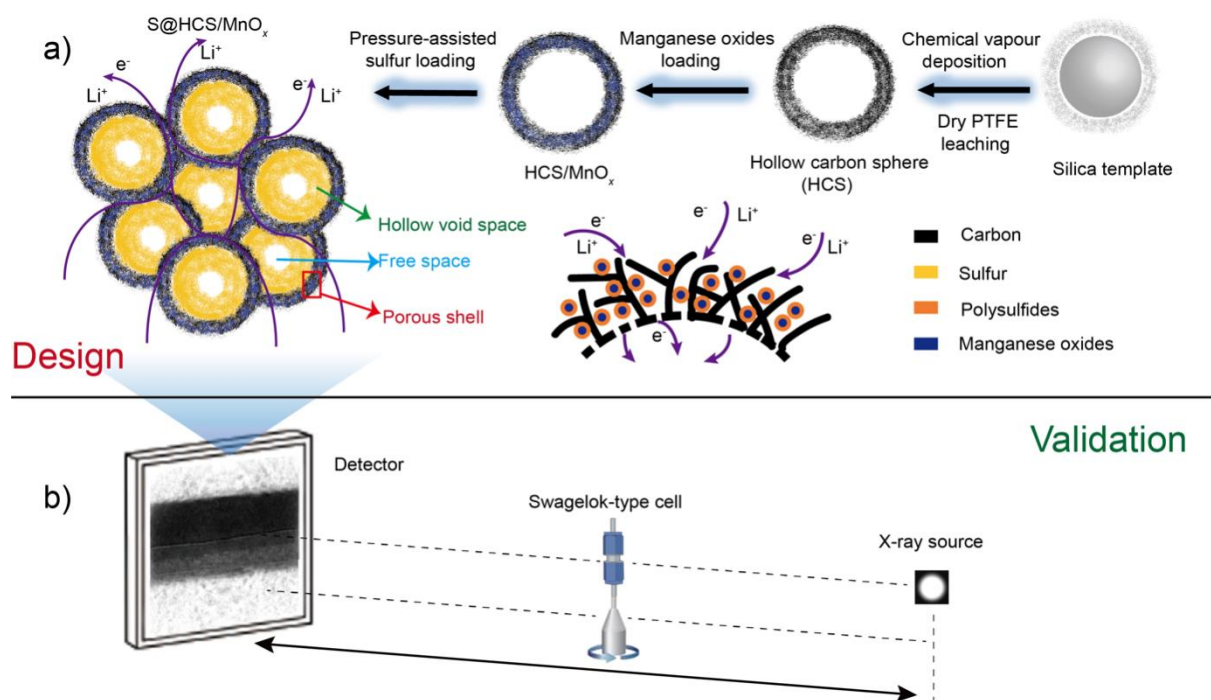


**Fig. 1** a) Schematic on the concept of S@HCS/MnO<sub>x</sub> electrode design. Each building block contains a hollow void and a mesoporous shell. The hollow void contains free space to accommodate sulfur volume expansion. The mesoporous structure maximizes the interaction between Li<sup>+</sup>, sulfur, manganese oxide and electrons. The hollow carbon spheres are synthesized via chemical vapor deposition (CVD) and polytetrafluoroethylene (PTFE) leaching. Manganese oxide nanoparticles are impregnated into the mesopores, while sulfur is loaded into both the voids and the mesopores. b) X-ray CT validates the effectiveness of the cathode design under *in situ* operation conditions with Swagelok cell.

In the S@HCS/MnO<sub>x</sub> cathode, the hollow void is encapsulated with a mesoporous shell that is loaded with manganese oxide (MnO<sub>x</sub>) particles, which can chemically trap the LiPSs.[31] Sulfur loading is maximized[32, 33] in both the void and the shell *via* a pressure-assisted impregnation.[34] The free space left in the void can accommodate sulfur volumetric expansion during discharge (**Fig. 1a**). In addition, the HCS is synthesized via a recently

developed liquid-free method,[35] which simultaneously achieves precise control over the HCS structure and reduces the operation cost. Manganese oxides ( $\text{MnO}_x$ ) nanoparticles with high surface polarity are loaded in HCS to provide chemical adsorption for polysulfide, and to enhance the electron transfer for polysulfides redox reaction.[36, 37] With the combination functions of carbon hollow structures and  $\text{MnO}_x$  nanoparticles, the  $\text{S@HCS/MnO}_x$  design addresses almost all the challenges in the Li-S cathode, which is proven by X-ray CT via tracing and analysing the active sulphur in the  $\text{S@HCS/MnO}_x$  cathode (**Fig. 1b**). After one discharge-charge cycle at a very low C-rate of 0.05, the  $\text{S@HCS/MnO}_x$  cathode retains 70% volume fraction of solid sulfur. In comparison, **only 5% volume fraction of solid sulfur particles** retains in the commercial S cathode, while most of the LiPSs shuttle across the separator and lose in the electrolyte. The  $\text{S@HCS/MnO}_x$  cathode shows very mild volume expansion of 16%, compared to 40% volume expansion in the commercial cathode. This is the first report on the direct visual evidence to prove the effectiveness of hollow structures in the stabilization of the active sulfur and confining cathode volume expansion during charge-discharge process.

## 2. Results and Discussion

### 2.1 Design of $\text{S@HCS/MnO}_x$ Cathode

The design concept includes spherical voids and mesoporous shells with sulfur loaded into both the voids and the shells while  $\text{MnO}_x$  nanoparticles confined inside the porous shells. Such configuration can effectively accommodate the sulfur volume expansion and maximize the interactions between active materials.

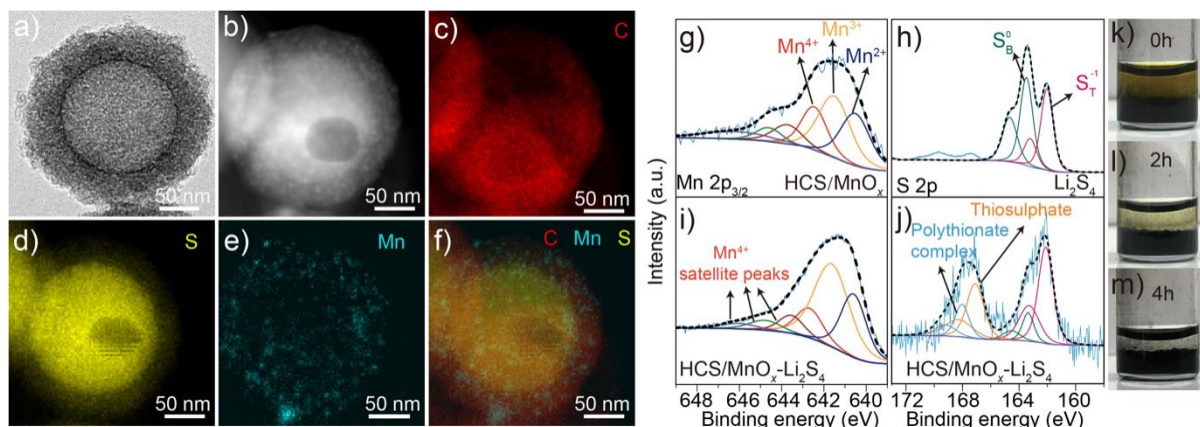


**Fig. 2** a) TEM images of HCS. b) dark field scanning TEM image of S@HCS/MnO<sub>x</sub> nanosphere. c-f) Energy-dispersive X-ray spectroscopy (EDS) element mapping on C (c), S (d), Mn (e) and all three elements superimposed (f). g-j) Mn 2p XPS spectra of HCS/MnO<sub>x</sub> (g) and HCS/MnO<sub>x</sub>-Li<sub>2</sub>S<sub>4</sub> (i); S 2p XPS spectra of Li<sub>2</sub>S<sub>4</sub> (h) and HCS/MnO<sub>x</sub>-Li<sub>2</sub>S<sub>4</sub> (j). k-m) Visualized adsorption of Li<sub>2</sub>S<sub>4</sub> on HCS/MnO<sub>x</sub> powder within 4 hours.

Solid-SiO<sub>2</sub>@mesoporous-SiO<sub>2</sub> (SiO<sub>2</sub>@mSiO<sub>2</sub>) spheres are chosen as the hard template to realize the concept (**Fig. S1 a and b**). Chemical vapour deposition (CVD) of ferrocene into the SiO<sub>2</sub>@mSiO<sub>2</sub> leads to the formation of SiO<sub>2</sub>@Fe-carbon composites (**Fig. S1 c and d**).<sup>[35]</sup> During CVD, ferrocene is oxidized to ferricenium which reacts with the silanol groups on the surface of porous silica.<sup>[38]</sup> This strong interaction promotes the carbon deposition on the inner surface of SiO<sub>2</sub>@mSiO<sub>2</sub> templates, filling the mesopores on the shell. As a result, the total pore volume and Brunauer-Emmett-Teller (BET) specific surface area of the as-formed SiO<sub>2</sub>@Fe-carbon composites are 0.17 cm<sup>3</sup> g<sup>-1</sup> and 188.79 m<sup>2</sup> g<sup>-1</sup> respectively, only half the values of the SiO<sub>2</sub>@mSiO<sub>2</sub> (0.35 cm<sup>3</sup> g<sup>-1</sup> and 394.34 m<sup>2</sup> g<sup>-1</sup>) (**Fig. S2**). This indicates the successful carbon filling of the mesopore channels in the SiO<sub>2</sub>@mSiO<sub>2</sub> templates. The composites maintain the similar morphology of SiO<sub>2</sub>@mSiO<sub>2</sub>. The iron particles are uniformly distributed in the mesopores of SiO<sub>2</sub>@mSiO<sub>2</sub> templates as shown in transmission electron micrograph (TEM) image (**Fig. S1d**). **During polytetrafluoroethylene (PTFE)**

**leaching**, the Fe/C/SiO<sub>2</sub>@mSiO<sub>2</sub> composites react with PTFE according to the formula:  $0.5n \text{ SiO}_2 + (\text{CF}_2)_n \rightarrow 0.5n \text{ SiF}_4\uparrow + n \text{ CO}\uparrow$ , [39] resulting in monodisperse HCS (**Figs. 2a** and **S3**). The formation of only gaseous products leads to the instant separation of carbon during leaching. **Negligible Fe and trace amount of SiO<sub>2</sub> are found in the HCS, indicating the effectiveness of PTFE leaching, which is in good consistence with our previous study (Fig. S4) [35].** The average void diameter  $180 \pm 8$  nm and shell thickness  $40 \pm 3$  nm of HCS match well with the solid cores ( $174 \pm 6$  nm) and the mesoporous shells ( $38 \pm 3$  nm) in SiO<sub>2</sub>@mSiO<sub>2</sub>, showing a perfect inverse replication (**Fig. S3**). The uniform particle size enables the even granular distribution of sulfur. The BET surface area is  $806 \text{ m}^2 \text{ g}^{-1}$  with a total pore volume of  $0.55 \text{ cm}^3 \text{ g}^{-1}$  and average pore size of 4.3 nm (**Fig. S5a**), implying high porosity of the HCS. The Raman spectrum of HCS gives a  $I_D/I_G$  ratio of 2.1, which is lower than that of commercial super P carbon (2.3), suggesting a large graphitic domain (**Fig. S5b**). [40, 41] This stems from the iron catalyzed carbon graphitization during PTFE leaching. To prove this, a smaller graphitic domain is obtained when Fe is removed by HCl prior to the PTFE leaching (**Fig. S5b**). The large graphitic domain in HCS provides high electrical conductivity and chemical stability required for the application in energy storage systems.

MnO<sub>x</sub> nanoparticles are loaded into the mesoporous shell *via* wetness impregnation, enabling their uniform distribution with an average size of  $3.5 \pm 2.0$  nm (**Figs. 2b-f** and **S6**). The MnO<sub>x</sub> nanoparticles with such small sizes have a larger active specific surface area than that of MnO<sub>x</sub> nanosheet structures, which contribute to efficient adsorption of LiPSs. [42, 43] The chemical interaction between HCS/MnO<sub>x</sub> and LiPSs was examined with Mn 3P<sub>3/2</sub> and S 2P X-ray photoelectron spectroscopy (XPS, **Fig. 2g-j**). The Mn 3P<sub>3/2</sub> peaks at 641.6 and 640.5 eV correspond to the Mn(III) and Mn(II) valence state. This is consistent with X-ray diffraction (XRD) patterns with diffraction peaks fit well to the hausmannite-type Mn<sub>3</sub>O<sub>4</sub> (**Fig. S4**, JCPDS: 00-024-0734). An additional peak is observed at 642.5 eV in the XPS curve, which is related to the Mn(IV) valence state. Three Mn(IV) satellite peaks at higher binding

energies of 643.6, 644.7, and 645.9 eV are also visible (**Fig. 2g**).[37, 44] It is hypothesized that the Mn(IV) is detected from the oxidized surface of the Mn<sub>3</sub>O<sub>4</sub> particles. Thus, the correct Mn chemical state should be between Mn<sub>3</sub>O<sub>4</sub> and MnO<sub>2</sub>, which is then denoted as MnO<sub>x</sub> here. MnO<sub>x</sub> can effectively adsorb LiPSs due to the polar surface and the Mn(II/III/IV) redox pair. Mixing the HCS/MnO<sub>x</sub> powder into a Li<sub>2</sub>S<sub>4</sub> solution leads to a decrease in Li<sub>2</sub>S<sub>4</sub> concentration. This can be visualized *via* a colour change of the solution from yellow green to colourless in 4 hours (**Fig 2k-m**). The solution becomes slightly dusty due to the suspension of porous carbon for electrostatic reason.

Upon adsorption of Li<sub>2</sub>S<sub>4</sub> as the LiPSs representative, the relative intensities of the Mn(IV) peak and its satellite peaks decrease from 18% and 24% to 12% and 15%, respectively, while the relative intensity of Mn(III) increase from 33% to 48% (**Fig. 2** and **Table S1**). The result suggests the reduction from surface Mn(IV) to Mn(II)/(III) by Li<sub>2</sub>S<sub>4</sub>. In the sulfur XPS spectra, both the initial terminal sulfur peak (S<sub>t</sub><sup>-1</sup> at 162.0 eV) and the bridging sulfur peak (S<sub>B</sub><sup>0</sup> at 163.4 eV)[37] decrease, while two S 2p peaks at 167.1 and 168.1 eV appear after Li<sub>2</sub>S<sub>4</sub> adsorption (**Fig. 2h, j**). The combination of Mn and S XPS shows that the adsorbed Li<sub>2</sub>S<sub>4</sub> will be partly oxidized to the insoluble thiosulphate and the polythionate species on the surface of MnO<sub>x</sub>, which leads to the reduction of surface Mn. Their insolubility help inhibit the polysulfides dissolution into the electrolyte and control the deposition of Li<sub>2</sub>S.[37]

Sulfur is loaded into the HCS/MnO<sub>x</sub> *via* pressure assisted impregnation. The high pressure of 5 bar ensures that the melted sulfur penetrates the mesopores and enters the voids of HCS/MnO<sub>x</sub>. The dispersion of sulfur inside S@HCS/MnO<sub>x</sub> composite is visualized *via* EDS mapping (**Figs. 2c-f and S6**), showing the free space, the sulfur core and the sulfur inside the mesoporous shell. The sulfur content is 73.8 wt% (**Fig. S6c**) determined by thermogravimetric analysis (TGA). The rapid weight loss between 200 and 300 °C is due to the sulfur evaporation from the voids. The slow weight loss from 300 to 400 °C can be ascribed to the

release of sulfur confined within the mesopores in HCS.[45] XRD shows two sulfur typical peaks at  $2\theta = 23^\circ$  and  $28^\circ$ , corresponding to an *Fddd* orthorhombic structure (**Fig. S6d**).

## 2.2 Electrochemical performances of the S@HCS/MnO<sub>x</sub> cathode

Electrochemical performances were investigated for the fabricated S@HCS/MnO<sub>x</sub> cathode. First, cyclic voltammogram (CV) was tested to understand the redox behavior in the cathode. At a scan rate of  $0.05 \text{ mV s}^{-1}$ , all three CV curves show similar shapes with two cathodic peaks caused by the formation of high-order polysulfides and further reduction to Li<sub>2</sub>S<sub>2</sub>/Li<sub>2</sub>S, and one anodic peak corresponding to the oxidation of Li<sub>2</sub>S to polysulfides and sulfur (**Fig. 3a**). Compared with the S cathode, the S@HCS cathode shows lower overpotential of the polysulfides redox reaction and higher current at the same active material loading, which indicates an improved redox kinetics. This is due to the effective interconnection between carbon framework and active sulfur. The incorporation of MnO<sub>x</sub> nanoparticles increases the reduction peaks from 2.01 and 2.24 V to 2.06 and 2.29 V, respectively. The corresponding oxidation peak also shifts from 2.47 to 2.39 V. The shifts in the redox peaks indicate the improvement in reaction kinetics, suggesting the catalytic effect of MnO<sub>x</sub>, which accelerates the conversion from S<sub>8</sub> to Li<sub>2</sub>S. The superior kinetics of the S@HCS/MnO<sub>x</sub> cathode leads to better rate capability than S@HCS and S cathodes (**Fig. 3b**). The S@HCS/MnO<sub>x</sub> delivers discharge capacities of 1123, 963, 871, 724, 638 mAh g<sup>-1</sup> at rates of 0.1, 0.2, 0.5, 1 and 2 C, respectively. The capacity is recovered to 951 mAh g<sup>-1</sup> when the rate is reverted to 0.1 C. The active sulfur mass loading on the tested electrodes is about 1-1.5 mg cm<sup>-2</sup>, which is widely used in the literatures. **This value is lower than the expected loading of Li-S battery for the market. Nevertheless, we use the relevant sulfur loading that is similar to the reported valued in the literature in order to make the following X-ray CT tomography study representative and sensible to the academic research.**

We further compared the cycling performances of the Li-S cells with S@HCS/MnO<sub>x</sub>, S@HCS and S cathodes in coin cell configuration. The S@HCS/MnO<sub>x</sub> cathode shows an initial specific capacity of 1147 mAh g<sup>-1</sup> and the best stability with an average decay rate of 0.16% per cycle over 150 cycles at 0.1 C (**Fig. 3c**). In sharp contrast, the S@HCS and S cathodes decay rapidly with the rate of 0.33% and 0.64% per cycle over 150 cycles at 0.1 C. **Fig. 3d** shows the corresponding charge/discharge curves of S@HCS/MnO<sub>x</sub> cathode at 50th, 100th and 150th. And the overpotentials between charge and discharge plateau remain relatively stable with increasing the cycle number. Furthermore, S@HCS/MnO<sub>x</sub> still shows stable cycling performance with an average decay rate of 0.18% per cycle over 300 cycles when the current density increases to 0.2 C (**Fig. 3e**), indicating that the majority of sulfur particles are kept within the cathode after long cycles and hence greatly improve the cycling performance.

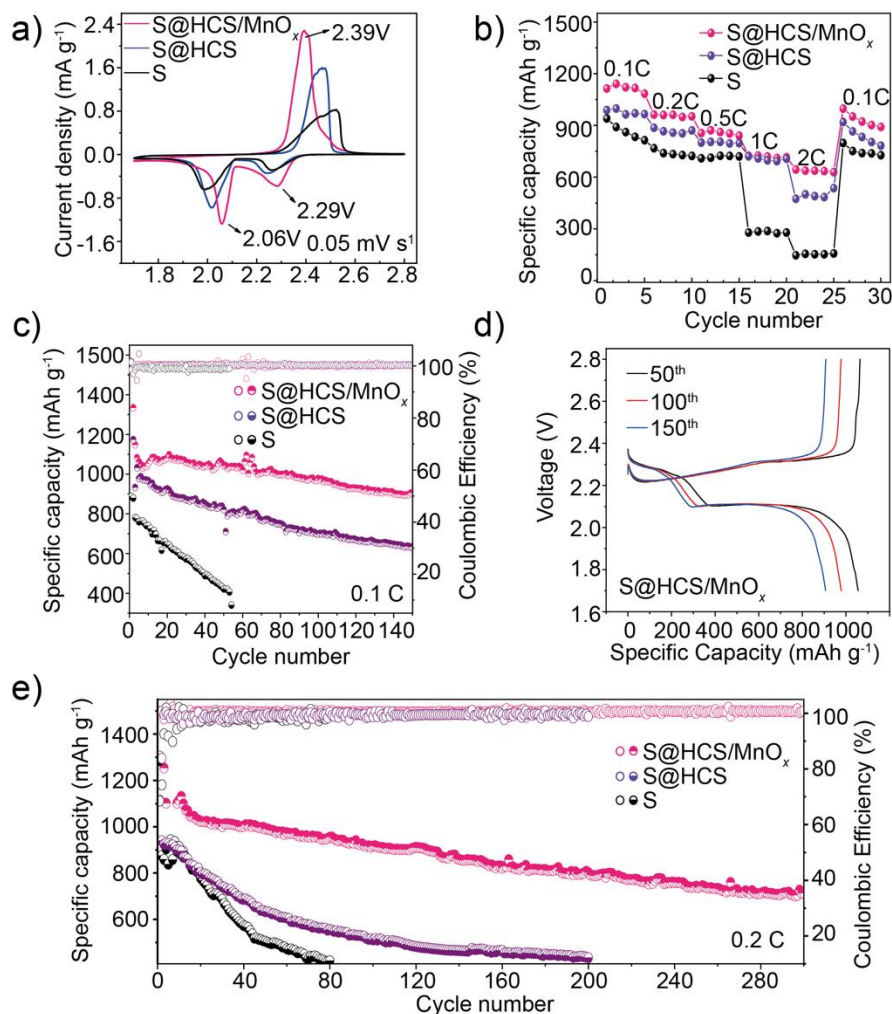


**Fig. 3** a) CV profiles of S@HCS/MnO<sub>x</sub> (red), S@HCS (purple) and S (black) electrodes at a scan rate of 0.05 mV/s. b) Rate performances between S@HCS/MnO<sub>x</sub> (red), S@HCS (purple) and S (black) electrodes. c-d) Cycling performances of S@HCS/MnO<sub>x</sub> (red), S@HCS (purple) and S (black) electrodes at rate of 0.1 C (c) and the corresponding charge-discharge profiles at 50th, 100th and 150th of S@HCS/MnO<sub>x</sub> (d). e) Long-term cycling performances of S@HCS/MnO<sub>x</sub> (red), S@HCS (purple) and S (black) electrodes at rate of 0.2 C.

### 2.3 Validation of S@HCS/MnO<sub>x</sub> cathode design

The above results demonstrate that the S@HCS/MnO<sub>x</sub> cathode can effectively accommodate sulfur expansion and immobilize LiPSs *via* free void space and polar MnO<sub>x</sub> surface, and also shows outstanding long-term electrochemical performance. Here, we employed X-ray CT

technology to carefully validate this design concept vis studying the cathode volume expansion and LiPSs shuttling for both S@HCS/MnO<sub>x</sub> and S cathodes. Such a non-destructive technique under *in situ* operation conditions enables tracking of thickness changes within the sulfur electrode, along with observation of the distribution and volume fraction of sulfur between a pristine Li-S cell and cycled cell. At the end of discharge state, as-formed Li<sub>2</sub>S and amorphous short-chain polysulfide have low X-ray attenuation coefficient leading a similar grayscale (brightness) to carbon and binder domains. Therefore, it is unable to quantify the main products at end of discharge state through segmentation by using micro-scale CT. Therefore, X-ray CT measurements were taken before and after cell undergoing one discharge/charge cycle at a very low C-rate. During the measurement, the as-prepared sulfur electrode, a Celgard separator and Li foil were assembled in a 1/8-inch bespoke polyether ether ketone (PEEK) Swagelok cell (**Fig. 4a**).<sup>[46]</sup> The active sulfur loading on the testing electrodes was 1.3 mg cm<sup>-2</sup> with the thickness of around 30 μm, which is the proper thickness for X-ray CT measurements. At high sulfur loading, the absolute volume expansion is larger than the volume allowed in the CT cell. The 2D virtual slices of pristine S@HCS/MnO<sub>x</sub> and commercial S electrodes (**Figs. 4b** and **d**) obtained from the X-ray CT scans clearly show three distinct layers according to the difference in grey scales. They are carbon-coated aluminium foil current collector, the as-prepared sulfur electrode and Celgard separator. The thickness of S@HCS/MnO<sub>x</sub> is varied within 3 μm, due to the introduced errors from manually coating. The thickness of each component was measured in 3D by the summation of all the voxels corresponding to each layer in MATLAB 2019a (**Fig. 4f**). The current collector and Celgard separator in both Li-S cells have similar thickness of 11 ± 1 and 23 ± 2 μm, respectively. However, the initial S@HCS/MnO<sub>x</sub> and S electrodes have different thickness of 25 and 35 μm, respectively, at the same sulfur loading of 1.3 mg cm<sup>-2</sup>. The volume fraction of solid sulfur particles to the whole electrode is in range of 0.20 to 0.37 for S@HCS/MnO<sub>x</sub> at different depth of the cathode, which is again lower than the value for S electrode (0.27 to

0.45) (**Fig. 4k**). These indicate that sulfur in the S@HCS/MnO<sub>x</sub> distributes more compactly and densely than that in the S cathode. In addition, the sulfur particles in the S@HCS/MnO<sub>x</sub> cathode are granularly distributed cross the electrode, as determined by the 3D volume-rendering of sulfur (**Fig. 4g**). This is in consistent with the sulfur EDS mapping (**Fig. 2**) in the STEM, showing the uniform encapsulation of sulfur within the carbon sphere, thus leading to the uniform distribution of sulfur over the whole cathode. In comparison, the 3D volume-rendering result suggests a non-uniform distribution of sulfur in the S cathode (**Fig. 4i**).

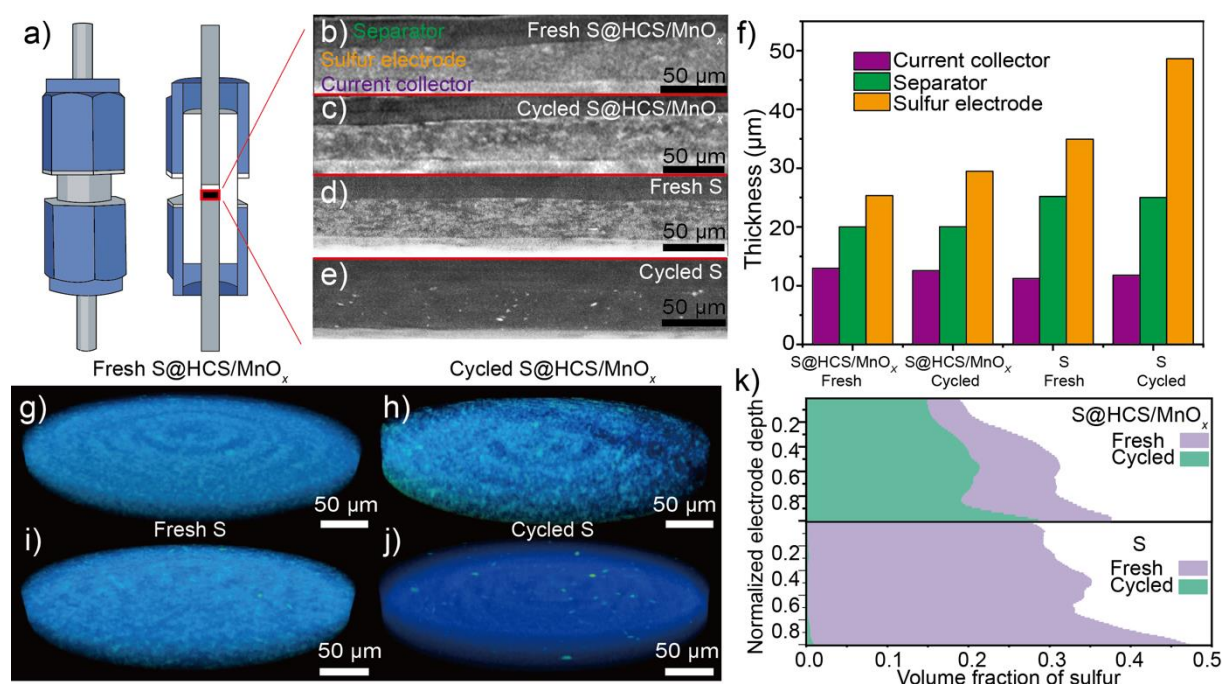


**Fig. 4** a) Schematic diagram and cutaway view of 1/8 inch (polyether ether ketone) PEEK Swagelok-type cell. b-e) 2D virtual slices from tomography images of Li-S cell with (b) fresh S@HCS/MnO<sub>x</sub> electrode; (c) S@HCS/MnO<sub>x</sub> electrodes with one discharge/charge cycle at rate of 0.05 C; (d) fresh S electrode and (e) S electrode with one discharge/charge cycle at rate of 0.05 C. f) Thickness of current collector, separator and sulfur electrode before and after cycling. g-j) Volume-rendering of the sulfur phase for (g) fresh S@HCS/MnO<sub>x</sub> electrode; (h) cycled S@HCS/MnO<sub>x</sub> electrode; (i) fresh S electrode and (j) cycled S electrode. k) Volume fraction as a function of fresh and cycled S@HCS/MnO<sub>x</sub> and S electrode thickness normalized to (0, 1) between the fixed positions of separator and current collector,

respectively. For j,k), the cathode is still more X-ray attenuating than the anode, proving the existence of polysulfides dissolved in the electrode. Therefore, only the solid sulfur particles larger than five times of the spatial resolution are safely quantified in the cycled S cell and the rest dissolved polysulfides is regarded as background.

The Li-S cells were discharged and charged over one cycle at a very low rate of 0.05 C to ensure the full conversion of sulfur to  $\text{Li}_2\text{S}$  and *vice versa*. After cycling, the thickness of the S@HCS/ $\text{MnO}_x$  electrode increases to 29  $\mu\text{m}$  from 25  $\mu\text{m}$  (**Fig. 4f**), indicating 16% volume expansion, and around 70% volume fraction of solid sulfur particles remain in the electrode (**Fig. 4k**). In comparison, over 40% volume expansion to 49  $\mu\text{m}$  is observed for this S electrode which we hypothesize to be attributable to the formation of  $\text{Li}_2\text{S}$  upon discharge [9, 47]. Unlike the S@HCS/ $\text{MnO}_x$  cell, the amount of sulfur particles significantly decreases in the cycled S electrode as they shuttle across the separator and failed to precipitate after the charging process. As a result, only 5% volume fraction of solid sulfur particles is remained in the cathode (**Fig. 4e and j**). To be clearly, the amorphous polysulfides and  $\text{Li}_2\text{S}$  are unable to quantified into sulfur volume fraction due to their low density and X-ray attenuation coefficient. Moreover, The boundary between S electrode and separator in figure 4e is not distinct due to the rest 95% are amorphous sulfur, sulfides and carbon, which have similar grayscale (brightness) to the polypropylene/polyethylene separator due to the similar X-ray attenuation coefficient and low density [46]. No structure collapse was observed for both S and S@HCS/ $\text{MnO}_x$  electrode due to the fine particle size of active sulfur and good mechanical stability of HCS [48].

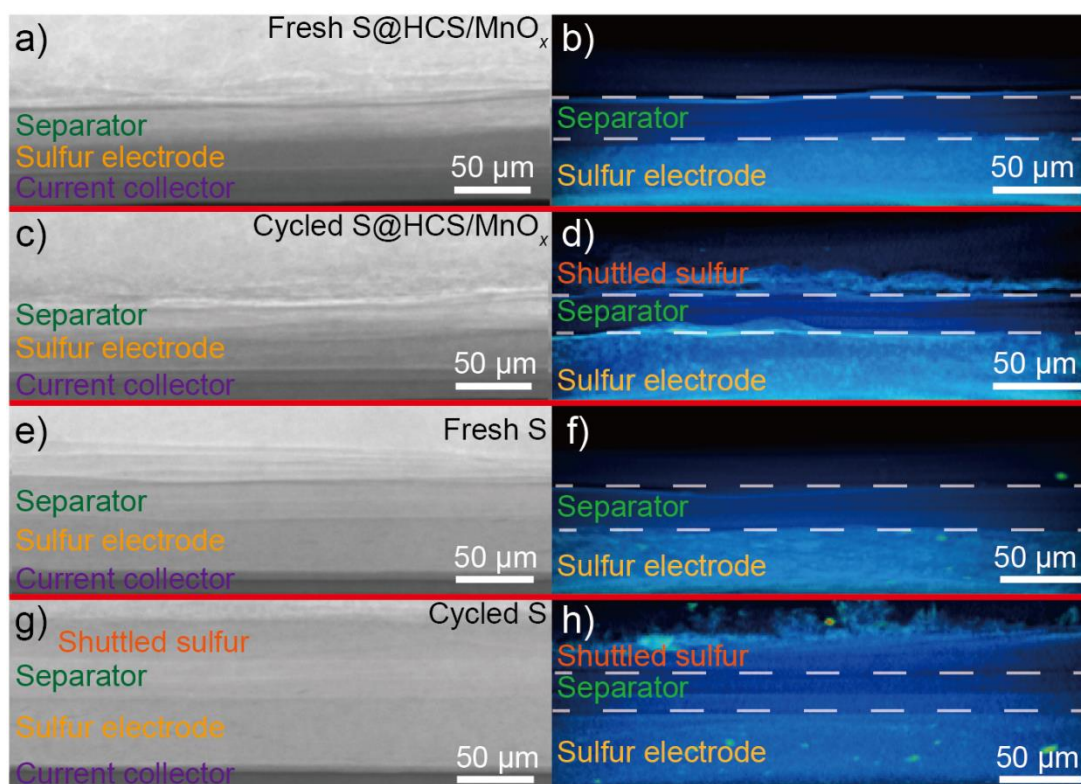


**Fig. 5** a-d) 2D radiographic and 3D volume rendering from tomography images of S@HCS/MnO<sub>x</sub> electrode before (a,b) and after (c,d) one discharge/charge cycle at rate of 0.05 C. e-h) 2D radiographic and 3D volume rendering from tomography images of S electrode before (e, f) and after (g, h) one discharge/charge cycle at rate of 0.05 C.

To further understand the LiPSs shuttling in both Li-S cells, 2D radiographic imaging and the 3D tomography were applied. The boundaries between current collector, sulfur electrode and separator are clearly shown and reveal the shuttling of sulfur across the separator (**Fig. 5**). For the S@HCS/MnO<sub>x</sub> electrode, a few floccules of sulfur are observed on the top side of the separator after cycling, while the majority of sulfur particles are kept within the cathode (**Fig. 5d**). In comparison, the cycled S cell clearly shows a thick shuttled sulfur layer in the vicinity of the separator with the thickness of 30 μm in both 2D radiographic image and 3D images (**Fig. 5g and h**). This is because of that the dissolved polysulfide intermediates shuttle to the Li metal anode where they can be reduced to short-chain polysulfides/Li<sub>2</sub>S and stay in the

electrolyte or become solid products to participate in the formation of the solid electrolyte interface on the Li metal anode [9, 49]. Moreover, the polysulfides can gradually etch the Li and cause a porous surface [50-52]. However, the morphology information of Li metal cannot be determined by X-ray CT here due to its low density and X-ray attenuation coefficient.

The combination of morphology and statistical deviation studies *via* X-ray CT proves the design concept of the S@HCS/MnO<sub>x</sub> cathode. To the best of our knowledge, the present X-ray CT study is the first attempt in tracking structural evolution of nano-designed hollow materials in the electrode. The results demonstrate that, in the micro-scale electrode, the design of porous shell and hollow structure of S@HCS/MnO<sub>x</sub> can effectively confine active sulfur and prevent volume expansion after cycling; furthermore, the MnO<sub>x</sub> nanoparticles and mesoporous shell can provide both chemically and physically confinement of polysulfide species.

### 3. Conclusion

In this work, we fabricate a novel S@HCS/MnO<sub>x</sub> cathode to achieve sulfur stabilization and LiPSs immobilization and further prove the design concept by X-ray CT technique. Via *in situ* visualization of X-ray CT, we find that only 16% volume expansion occurs in S@HCS/MnO<sub>x</sub> after cycling and 70% volume fraction of solid sulfur remains in the cathode. Such a cathode design can overcome two major challenges, *i.e.*, volume expansion and shuttle effect of LiPSs. As a result, the S@HCS/MnO<sub>x</sub> cathode delivers a specific capacity as high as 1100 mAh g<sup>-1</sup> at 0.2 C with a fade rate of 0.18% per cycle over 300 cycles, which are among the best of reported HCS/S electrodes. Moreover, the developed X-ray CT is demonstrated to be a vital tool in visualizing microstructural evolution, which bridges the gap between fundamental research and the real situation at cell level. The ability to trace active sulphur across the electrodes and electrolyte is crucial for developing high-performance Li-S batteries as well as other energy storage systems.

### 4. Experimental Section

***Synthesis of SiO<sub>2</sub>@mSiO<sub>2</sub> template.*** To synthesis SiO<sub>2</sub> core, ethanol (552.3 g), H<sub>2</sub>O (132.53 ml), NH<sub>3</sub> (28-30%, 12.83 ml) and tetraethyl orthosilicate (TEOS, 27.77 ml) were mixed and then stirred for 12 hours at room temperature. To obtain mesoporous shell, TEOS (19.72 ml) and octadecyltrimethoxysilane (OTMS, 7.78 ml) were then added to the mixture. The mixture was then stirred for another 12 hours. The product was collected by centrifugation and dried at 60 °C. The sample was calcined at 550 °C for 1.5 h to remove the alkyl chains contained in OTMS.

***Synthesis of hollow carbon sphere (HCS).*** The chemical vapor deposition (CVD) method was applied to synthesise HCS. The obtained SiO<sub>2</sub>@mSiO<sub>2</sub> template and ferrocene were used as template and carbon source, respectively. Ferrocene (2g) and SiO<sub>2</sub>@mSiO<sub>2</sub> (500 mg) were placed in different heating zones within the two-stage tubular furnace. The sublimation and the pyrolysis of the ferrocene were conducted at 120 and 550 °C, respectively, with an argon flow rate of 56 ml min<sup>-1</sup>. The as-prepared Fe-carbon@SiO<sub>2</sub> composite (500 mg) was mixed with PTFE (4 g) and heated under 1 L min<sup>-1</sup> nitrogen flow at 900 °C for 4 h to subsequently leach silica.

***Synthesis of S@HCS/MnO<sub>x</sub> electrode material.*** To load the MnO<sub>x</sub> particles into HCS, Mn(NO<sub>3</sub>)<sub>2</sub> (50wt% in dilute nitric acid, 50 µl) was impregnated into HCS powder (100 mg) under stirring until mixed uniformly, then dried at 60 °C. The mixture was heated at 250 °C under humidifying argon flow for 3 h. To dope sulfur, obtained mixture (50 mg) and sulfur (400 mg) were physically mixed together, then added into a Teflon inset. The mixture was transferred into a stainless-steel autoclave reactor, and then sealed and purged with nitrogen three times. The reaction was performed at 165 °C with 5 bar nitrogen pressure. The obtained powder was placed into furnace and heated at 200 °C for 1 h to remove surface sulfur.

***Polysulfides adsorption measurement.*** All the glass vials were dried in the oven for 24 hours before the experiment. The lithium sulfide (Li<sub>2</sub>S, 1.94 mg) and sulfur powder (S, 4.06 mg) were dissolved in 4 ml mixture of 1,3-dioxolane (DOL) and 1,2-dimethoxyethane (DME) (1:1

volume ration mixture) at 60 °C for 72 h. The dry HCS/MnO<sub>x</sub> powder (15mg) was put in obtained Li<sub>2</sub>S<sub>4</sub> solution for observation. After polysulfides adsorption, all the samples for XPS were prepared in an Ar-filled glovebox. Then the obtained HCS/MnO<sub>x</sub> powder was transferred from an Ar-filled glovebox to the XPS measurement chamber in a sealed sample bottle as soon as possible. The as-prepared Li<sub>2</sub>S<sub>4</sub> solution was put in clean Ar-filled glovebox without a lid to volatilize the DOL/DME solvent. The obtained Li<sub>2</sub>S<sub>4</sub> powder was then transferred to the XPS measurement chamber in a sealed sample bottle as soon as possible.

**Electrochemical measurements.** All of the electrochemical measurements were tested on 2032-type coin cells with lithium foil as the anode. The 1/8-inch PEEK Swagelok cell was assembled with the sulfur electrode laser-cut to 2 mm diameter as the positive electrode, and Li foil punched to 1.5 mm diameter as the negative electrode. Stainless steel plungers provided compression and electrical connection. The electrolyte was LiTFSI (1 mol L<sup>-1</sup>) in a mixed solution of 1,2-dimethoxyethane (DME) and 1,3-dioxolane (DOL) (1:1 v/v) with LiNO<sub>3</sub> (2 wt%) as the additive. The amount of electrolyte added to each coin cell was 20 μl/mg<sub>sulfur</sub>. To prepare the cathode electrode, the obtained sulfur composites (80 mg), super P (10 mg), sodium carboxyl methyl cellulose (NaCMC, 5 mg) and styrene butadiene rubber (SBR, 5 mg) were dispersed in deionized water. The slurry was coated onto aluminium foil and dried at 80 °C overnight under vacuum. The as-prepared electrode was cut in a circular shape with diameter of 8mm and sulfur loading is 1-1.5 mg cm<sup>-2</sup>. The sulfur cathode was prepared in the same way. CV measurements were carried out using an electrochemical workstation (CHI614b) at scan range of 0.05 mV s<sup>-1</sup> with potential range from 1.7 to 2.8 V vs Li/Li<sup>+</sup> at room temperature. The galvanostatic charge and discharge rates were tested in the voltage range from 1.7 to 2.8 V vs Li/Li<sup>+</sup> with different current densities by using a battery measurement system (Land China).

**Characterization.** XRD measurement was performed using a StadiP diffractometer from STOE, a voltage of 40 kV, at 30 mA, using a Cu source with Kα<sub>1</sub> = 1.540562 Å and Kα<sub>2</sub> =

1.544398 Å. The signal from  $K\alpha_2$  was removed for analysis. XPS was performed on a Thermo Scientific XPS K-alpha surface analysis machine using an Al source. Nitrogen adsorption–desorption isotherms were recorded at 77 K using a Micromeritics 3Flex surface characterization analyser. The samples were degassed at 300 °C overnight. Specific surface areas were determined according to the BET model, with pore diameters, volumes and distributions determined through the BJH method. TEM was observed using a JEOL JEM–2100 microscope equipped with an Oxford Instruments EDS detector at 200 kV. Particle size distributions were estimated through measurement of 100 particles. SEM imaging was performed on a JEOL JSM-7401F SEM. Scanning transmission electron microscopy (STEM) was performed using a CS-corrected Hitachi HD-2700 dedicated STEM equipped with detectors for bright-field (BF), high-angle annular dark-field (HAADF) and secondary electron (SE) imaging at 200 kV.

The assembled Swagelok cell before and after the cycling test was imaged on a Zeiss Xradia Versa 520 X-ray microscope operated at 100 kV (Carl Zeiss XRM, CA, USA).[53] The source-to-sample and sample-to-detector distances are 16 and 14 mm respectively, combined with a 40x optical magnification lens, giving a voxel size of  $0.36 \times 0.36 \times 0.36 \mu\text{m}^3$  and a field-of-view (FOV) of  $360 \times 360 \mu\text{m}^2$ . X-ray projections were collected every 30 seconds during angular rotation over the full  $180^\circ$  scan, with a step size of  $0.15^\circ$  giving 2401 projections. These radiographic projections were then reconstructed by a proprietary Feldkamp-Davis-Kress (FDK) algorithm in the Zeiss Xradia XMReconstructor software.[54] Images segmentation and volume fraction analysis of the electrode component was conducted using Avizo 9.4 (Thermo Fisher Scientific, UK). To measure the volume fraction of S, the reconstructed grayscale data were first segmented into S and non-S phases based on the distinct difference of gray values (i.e. brightness). The volume fraction was then calculated by dividing the total number of the voxels that represent S to the sum of the voxels of the cathode. The grayscale range used to segment solid S in the fresh and cycled samples was kept

**consistent.** The thickness of different electrode layers was quantified using MATLAB script by counting the constitutive voxels of the segmented data in depth direction.

### **Supporting Information**

Supplementary data to this article can be found online.

### **Conflicts of interest**

The authors declare no competing interests.

### **Acknowledgements**

R. X and J. X contributed equally to this work. The project is funded by EPSRC (EP/P02467X/1 EP/S018204/1 and EP/N032888/1), Royal Society (RG160661, IES\R3\170097), the Newton Fellowship (NF170761), and the National Natural Science Foundation of China (51632001). We acknowledge Diamond Light Source beamtime (EM17559, EM19318, EM19246 and EM20643). P.R.S acknowledges the support of the Royal Academy of Engineering. R. X would like to thank the China Scholarship Council (CSC) for the PhD funding.

## References

- [1] S. Gu, C. Sun, D. Xu, Y. Lu, J. Jin, Z. Wen, *Electrochem. Energy Rev.* 1 (2018) 599-624.
- [2] X. Yang, X. Li, K. Adair, H. Zhang, X. Sun, *Electrochem. Energy Rev.* 1 (2018) 239-293.
- [3] P.G. Bruce, S.A. Freunberger, L.J. Hardwick, J.-M. Tarascon, *Nat. Mater.* 11 (2012) 19.
- [4] L. Fan, M. Li, X. Li, W. Xiao, Z. Chen, J. Lu, *Joule* (2019).
- [5] H. Yuan, W. Zhang, J.-G. Wang, G. Zhou, Z. Zhuang, J. Luo, H. Huang, Y. Gan, C. Liang, Y. Xia, *Energy Storage Mater.* 10 (2018) 1-9.
- [6] X. Yang, J. Luo, X. Sun, *Chem. Soc. Rev.* 49 (2020) 2140-2195.
- [7] X. Li, M. Banis, A. Lushington, X. Yang, Q. Sun, Y. Zhao, C. Liu, Q. Li, B. Wang, W. Xiao, *Nat. Commun.* 9 (2018) 1-10.
- [8] X. Yang, Y. Chen, M. Wang, H. Zhang, X. Li, H. Zhang, *Adv. Funct. Mater.* 26 (2016) 8427-8434.
- [9] Y. Yang, G. Zheng, Y. Cui, *Chem. Soc. Rev.* 42 (2013) 3018-3032.
- [10] X.L. Ji, L.F. Nazar, *J. Mater. Chem.* 20 (2010) 9821-9826.
- [11] Q. Pang, C.Y. Kwok, D. Kundu, X. Liang, L.F. Nazar, *Joule* 3 (2019) 136-148.
- [12] Z. Li, B.Y. Guan, J. Zhang, X.W.D. Lou, *Joule* 1 (2017) 576-587.
- [13] C. Zhang, Q.-H. Yang, *Sci. China Mater.* 58 (2015) 349-354.
- [14] Y. Tian, G. Li, Y. Zhang, D. Luo, X. Wang, Y. Zhao, H. Liu, P. Ji, X. Du, J. Li, *Adv. Mater.* 32 (2020) 1904876.
- [15] Y. Tian, Y. Zhao, Y. Zhang, L. Ricardez-Sandoval, X. Wang, J. Li, *Appl. Mater. Interfaces* 11 (2019) 23271-23279.
- [16] L. Zhang, M. Ling, J. Feng, L. Mai, G. Liu, J. Guo, *Energy Storage Mater.* 11 (2018) 24-29.
- [17] X. Chen, T.-Z. Hou, B. Li, C. Yan, L. Zhu, C. Guan, X.-B. Cheng, H.-J. Peng, J.-Q. Huang, Q. Zhang, *Energy Storage Mater.* 8 (2017) 194-201.
- [18] X. Yang, X. Gao, Q. Sun, S.P. Jand, Y. Yu, Y. Zhao, X. Li, K. Adair, L.Y. Kuo, J. Rohrer, *Advanced Materials* 31 (2019) 1901220.
- [19] G. Zheng, Y. Yang, J.J. Cha, S.S. Hong, Y. Cui, *Nano Lett.* 11 (2011) 4462-4467.
- [20] F. Pei, T. An, J. Zang, X. Zhao, X. Fang, M. Zheng, Q. Dong, N. Zheng, *Adv. Energy Mater.* 6 (2016) 1502539.
- [21] M. Xiang, H. Wu, H. Liu, J. Huang, Y. Zheng, L. Yang, P. Jing, Y. Zhang, S. Dou, H. Liu, *Adv. Funct. Mater.* 27 (2017) 1702573.
- [22] J. Zhao, G. Zhou, K. Yan, J. Xie, Y. Li, L. Liao, Y. Jin, K. Liu, P.C. Hsu, J. Wang, H.M. Cheng, Y. Cui, *Nat. Nanotechnol.* 12 (2017) 993-999.
- [23] Y. Wang, R. Zhang, Y.-c. Pang, X. Chen, J. Lang, J. Xu, C. Xiao, H. Li, K. Xi, S. Ding, *Energy Storage Mater.* 16 (2019) 228-235.
- [24] X. Gao, X. Yang, M. Li, Q. Sun, J. Liang, J. Luo, J. Wang, W. Li, J. Liang, Y. Liu, *Adv. Funct. Mater.* 29 (2019) 1806724.
- [25] X. Yang, H. Zhang, Y. Chen, Y. Yu, X. Li, H. Zhang, *Nano Energy* 39 (2017) 418-428.
- [26] P.R. Shearing, J. Golbert, R.J. Chater, N.P. Brandon, *Chem Eng Sci.* 64 (2009) 3928-3933.
- [27] X.K. Lu, T. Li, A. Bertei, J.I.S. Cho, T.M.M. Heenan, M.F. Rabuni, K. Li, D.J.L. Brett, P.R. Shearing, *Energy Environ. Sci.* 11 (2018) 2390-2403.
- [28] Q. Meyer, N. Mansor, F. Iacoviello, P.L. Cullen, R. Jervis, D. Finegan, C. Tan, J. Bailey, P.R. Shearing, D.J.L. Brett, *Electrochim. Acta* 242 (2017) 125-136.
- [29] S.J. Cooper, D.S. Eastwood, J. Gelb, G. Damblanc, D.J.L. Brett, R.S. Bradley, P.J. Withers, P.D. Lee, A.J. Marquis, N.P. Brandon, P.R. Shearing, *J. Power Sources* 247 (2014) 1033-1039.
- [30] P.R. Shearing, N.P. Brandon, J. Gelb, R. Bradley, P.J. Withers, A.J. Marquis, S. Cooper, S.J. Harris, *J. Electrochem. Soc.* 159 (2012) A1023-A1027.

- [31] W.B. Kong, L.J. Yan, Y.F. Luo, D.T. Wang, K.L. Jiang, Q.Q. Li, S.S. Fan, J.P. Wang, *Adv. Funct. Mater.* 27 (2017) 1606663.
- [32] N. Jayaprakash, J. Shen, S.S. Moganty, A. Corona, L.A. Archer, *Angew. Chem. Int. Ed.* 50 (2011) 5904-5908.
- [33] D.W. Wang, Q.C. Zeng, G.M. Zhou, L.C. Yin, F. Li, H.M. Cheng, I.R. Gentle, G.Q.M. Lu, *J. Mater. Chem. A* 1 (2013) 9382-9394.
- [34] A. Gallas-Hulin, J. Mielby, S. Kegnaes, *ChemistrySelect* 1 (2016) 3942-3945.
- [35] R. Xu, L. Kang, J. Knossalla, J. Mielby, Q. Wang, B. Wang, J. Feng, G. He, Y. Qin, J. Xie, A.C. Swertz, Q. He, S. Kegnaes, D.J.L. Brett, F. Schuth, F.R. Wang, *ACS Nano* 13 (2019) 2463-2472.
- [36] Q. Pang, D. Kundu, M. Cuisinier, L. Nazar, *Nat. Commun.* 5 (2014) 4759.
- [37] X. Liang, C. Hart, Q. Pang, A. Garsuch, T. Weiss, L.F. Nazar, *Nat. Commun.* 6 (2015) 5682.
- [38] M.C. Schnitzler, A.S. Mangrich, W.A. Macedo, J.D. Ardisson, A.J. Zarbin, *Inorg. Chem.* 45 (2006) 10642-10650.
- [39] D.K. Singh, K.S. Krishna, S. Harish, S. Sampath, M. Eswaramoorthy, *Angew. Chem. Int. Ed.* 55 (2016) 2032-2036.
- [40] J.P. Tessonnier, D. Rosenthal, T.W. Hansen, C. Hess, M.E. Schuster, R. Blume, F. Girgsdies, N. Pfander, O. Timpe, D.S. Su, R. Schlogl, *Carbon* 47 (2009) 1779-1798.
- [41] R. Huang, J.Y. Xu, J. Wang, X.Y. Sun, W. Qi, C.H. Liang, D.S. Su, *Carbon* 96 (2016) 631-640.
- [42] W. Sun, X. Ou, X. Yue, Y. Yang, Z. Wang, D. Rooney, K. Sun, *Electrochim. Acta* 207 (2016) 198-206.
- [43] X. Zhao, H. Wang, G. Zhai, G. Wang, *Chemistry* 23 (2017) 7037-7045.
- [44] X. Chen, L. Yuan, Z. Hao, X. Liu, J. Xiang, Z. Zhang, Y. Huang, J. Xie, *Acs Appl. Mater. Interfaces* 10 (2018) 13406-13412.
- [45] J.J. Zhou, Y.S. Guo, C.D. Liang, J. Yang, J.L. Wang, Y.N. Nuli, *Electrochim Acta* 273 (2018) 127-135.
- [46] C. Tan, T.M. Heenan, R.F. Ziesche, S.R. Daemi, J. Hack, M. Maier, S. Marathe, C. Rau, D.J. Brett, P.R. Shearing, *ACS Appl. Energ. Mater.* 1 (2018) 5090-5100.
- [47] Y. Liu, J. Guo, J. Zhang, Q. Su, G. Du, *Appl. Surf. Sci.* 324 (2015) 399-404.
- [48] M. Lécuyer, J. Gaubicher, M. Deschamps, B. Lestriez, T. Brousse, D. Guyomard, *J. Power Sources* 241 (2013) 249-254.
- [49] C.H. Chang, S.H. Chung, A. Manthiram, *Small* 12 (2016) 174-179.
- [50] X.-B. Cheng, C. Yan, X. Chen, C. Guan, J.-Q. Huang, H.-J. Peng, R. Zhang, S.-T. Yang, Q. Zhang, *Chem* 2 (2017) 258-270.
- [51] X. Liang, Z. Wen, Y. Liu, M. Wu, J. Jin, H. Zhang, X. Wu, *J. Power Sources* 196 (2011) 9839-9843.
- [52] C. Yan, X.-B. Cheng, C.-Z. Zhao, J.-Q. Huang, S.-T. Yang, Q. Zhang, *J. Power Sources* 327 (2016) 212-220.
- [53] R. Schurch, S.M. Rowland, R.S. Bradley, P.J. Withers, *IEEE. T. Dielect. El. In.* 22 (2015) 709-719.
- [54] P. Prakash, M.K. Kalra, A.K. Kambadakone, H. Pien, J. Hsieh, M.A. Blake, D.V. Sahani, *Investing. Radiol.* 45 (2010) 202-210.